



Glycosylated zinc phthalocyanine-gold nanoparticle conjugates for photodynamic therapy: Effect of nanoparticle shape

Edith Dube, David O. Oluwole, Njemuwa Nwaji, Tebello Nyokong*

Center for Nanotechnology Innovation, Department of Chemistry, Rhodes University, Grahamstown 6140, South Africa

ARTICLE INFO

Article history:

Received 13 October 2017

Received in revised form 25 May 2018

Accepted 26 May 2018

Available online 28 May 2018

Keywords:

Glycosylation

Zinc phthalocyanine

Photodynamic therapy

Gold nanoparticles

ABSTRACT

In this work, we report on the synthesis of tris-[(2,2,7,7-tetramethyltetrahydro-3aH-bis([1,3]dioxolo)[4,5-b:4',5'-d]pyran-5-yl)methoxy)-2-(4-benzo[d]thiazol-2-ylphenoxyphthalocyaninato) zinc(II) (complex **3**) and its linkage to gold nanoparticles (AuNPs) of different shapes through S-Au/N-Au self-assembly. The conjugates of complex **3** (with both gold nanorods (AuNR) and nanospheres (AuNS)), displayed decreased fluorescence quantum yield with corresponding improved triplet and singlet quantum yields compared to complex **3** alone, however **3**-AuNR showed improved properties than **3**-AuNS. Complex **3** showed relatively low *in vitro* dark cytotoxicity against the epithelial breast cancer cells with cell survival $\geq 85\%$ at concentration $\leq 160 \mu\text{g/mL}$ but afforded reduced photodynamic therapy activity which may be due to aggregation. **3**-AuNR afforded superior PDT activity with $<50\%$ viable cells at concentration $\geq 40 \mu\text{g/mL}$ in comparison to **3**-AuNS with $<50\%$ viable cells at concentration $\geq 80 \mu\text{g/mL}$. The superior activity of **3**-AuNR is attributed to the photothermal therapy effect since nanorods absorb more light at 680 nm than nanospheres.

© 2018 Elsevier B.V. All rights reserved.

1. Introduction

Photodynamic therapy (PDT) involves the systemic administration of a suitable photosensitizer (PS), followed by activation of the localized PS in the tumor by light of a specific wavelength. The excited triplet state of the PS then transfers its energy to the ground state molecular oxygen resulting in the production of singlet oxygen which is the main cytotoxic species responsible for the cidal of unhealthy cells [1]. Metallophthalocyanines (MPcs) are a class of dyes used in various fields, such as in nonlinear optics [2], photodynamic therapy (PDT) [3,4], and photodynamic antimicrobial chemotherapy (PACT) [5]. Their ability to efficiently generate singlet oxygen, ease of chemical modification and strong absorption in the near infrared region, make them viable and efficacious photosensitizers (PS) for photodynamic therapy [3].

Despite the many successes recorded for the PDT activity of MPcs, there remain some drawbacks which include lack of selectivity and specificity towards cancer cells in comparison to healthy ones. To address these drawbacks, various approaches such as: encapsulation of the PS in colloidal carriers (liposomes [6,7] or polymeric micelles [8,9]), and conjugation of the PS to antibodies [10,11], synthetic peptides [12–14], nanoparticles [15,16] and carbohydrates [17–22] have been explored.

Glycosylated MPcs are promising PS candidates for use in PDT. Cancer cells are reported to have an increased uptake for sugars and over-

express glucose transporter proteins due to their increased demand for metabolic energy [23–25]. An isopropylidene protected tetra β -glycosylated zinc(II) phthalocyanine was reported to have shown high uptake and photodynamic cytotoxicity in MCF-7 cells [22]. Hence, glycoconjugation of the PSs improves their membrane interaction and uptake by cancer cells, thus increasing tumor selectivity [17,26,27]. Additionally, carbohydrates improve water solubility, an important parameter for cellular uptake of the PSs [17,28].

On the other hand, low symmetry MPcs offer greater advantages over their symmetrically substituted analogue due to possession of specific binding site for attachment to drug delivery agents [29]. The existence of different functional groups in low symmetry Pcs allow for the coexistence of several features in a molecule, and therefore an improvement in the Pc's properties.

Heterocyclic compounds containing sulphur and nitrogen, known as benzothiazole and their derivatives have been shown to possess good photosensitizing as well as anticancer activity [30,31]. In view of the photosensitizing importance of benzothiazoles and glycosylated phthalocyanines, a combination of these functional structures into one is expected to serve as potential PS for PDT. Apart from these, the sulphur and nitrogen in the benzothiazole ring will provide site for the non-covalent interaction of the phthalocyanine to metallic nanoparticles such as Au nanoparticles (AuNPs).

In this work, we report for the first time the synthesis of low symmetry tris-[(2,2,7,7-tetramethyltetrahydro-3aH-bis([1,3]dioxolo)[4,5-b:4',5'-d]pyran-5-yl)methoxy)-2-(4-benzo[d]thiazol-2-ylphenoxyphthalocyaninato) zinc(II) (complex **3**) as well as the

* Corresponding author.

E-mail address: tnyokong@ru.ac.za (T. Nyokong).

surface assembly of the synthesized complex onto different shapes of AuNPs: gold nanospheres (AuNS) and gold nanorods (AuNR), (whose syntheses has been reported before [32,33]). AuNR are of interest since they possess superior long blood circulation time due to the anisotropic geometry [34,35]. Complex **3** was linked to gold nanoparticles (AuNPs) through the S–Au or N–Au bond since gold is known for its affinity for sulphur and nitrogen (with the former being stronger than the latter). Phthalocyanines have been linked to AuNPs of different shapes before [32] with improved triplet state and singlet oxygen quantum yields as well as improved PDT activity [36]. This work reports for the first time on the linkage of AuNPs to glycosylated MPcs. The MPcs, NPs and the conjugates were characterized and the photophysical properties and PDT activity (against MCF-7 breast cancer cells) were studied.

2. Experimental

2.1. Materials

Ultra-pure water was obtained from a Milli-Q Water System (Millipore Corp, Bedford, MA, USA), 1-pentanol, zinc(II) acetate dihydrate, 1,8-diazobicyclo[5.4.0]undec-7-ene (DBU), unsubstituted zinc phthalocyanine (ZnPc), 1,3-diphenylisobenzofuran (DPBF) and anthracene-9,10-bis-methylmalonate (ADMA) were purchased from Sigma-Aldrich. Tetrahydrofuran (THF), toluene, and dimethyl sulphoxide (DMSO) were purchased from Merck. Methanol and absolute ethanol were obtained from SAARCHEM. All other reagents and solvents were obtained from commercial suppliers and used as received. Silica gel 60 (0.063–0.200 mm) for column chromatography was used for the purification processes. AlPcSmix (containing a mixture of sulfonated derivatives) was used as a standard for singlet oxygen quantum yields and was synthesized according to literature methods [37]. The syntheses of 4-glycosylated phthalonitrile (complex **1**) [22] and 4-(4-(benzo thiazol-2-yl)phenoxy) phthalonitrile (complex **2**) [38] have been reported in literature.

Cultures of epithelial breast cancer cells (MCF-7 cells) were obtained from Cellonex. Trypsin, human serum albumin (HSA), trypan blue, Dulbecco's phosphate-buffered saline (DPBS) and Dulbecco's modified Eagle's medium (DMEM) were obtained from Sigma Aldrich, heat-inactivated fetal calf serum (FCS), neutral red cell proliferation reagent (WST-1), and 100 µg/mL-penicillin-100 unit/mL-streptomycin-amphotericin B mixture were obtained from Biowest.

2.2. Equipment

Infrared spectra were acquired on a Bruker ALPHA FT-IR spectrometer with universal attenuated total reflectance (ATR) sampling accessory. ¹H NMR spectra were recorded on a Bruker AVANCE II 600 MHz NMR spectrometer using tetramethylsilane (TMS) as an internal reference. Elemental analyses were performed using a Vario-Elementar Microcube ELIII. Mass spectra data were collected on a Bruker AutoFLEX III Smart-beam TOF/TOF mass spectrometer using α-cyano-4-hydrocinnamic acid as the matrix. X-ray powder diffraction patterns were recorded using a Cu Kα radiation (1.5405 Å, nickel filter), on a Bruker D8 Discover equipped with a proportional counter and the data was processed using the Eva (evaluation curve fitting) software. The morphologies of the nanoparticles were assessed using a transmission electron microscope (TEM), ZEISS LIBRA model 120 operated at 90 kV and iTEM software was used for TEM micrographs processing. Elemental compositions of the NPs and the conjugates were qualitatively determined using energy dispersive X-ray spectroscopy (EDX), INCA PENTA FET coupled to the VAGA TESCAM operated at 20 kV accelerating voltage. Ground state electronic absorption was measured using a Shimadzu UV-2550 spectrophotometer. Fluorescence excitation and emission spectra were measured on a Varian Eclipse spectrofluorimeter using a 360–1100 nm filter. Excitation spectra were recorded using the

Q-band of the emission spectra. Fluorescence lifetimes were measured using a time correlated single photon counting setup (TCSPC) (FluoTime 300, Picoquant GmbH) with a diode laser (LDH-P-670, Picoquant GmbH, 20 MHz repetition rate, 44 ps pulse width). Details have been provided before [39].

Triplet quantum yields were determined using a laser flash photolysis system. The excitation pulses were produced using a tunable laser system consisting of an Nd:YAG laser (355 nm, 135 mJ/4–6 ns) pumping an optical parametric oscillator (OPO, 30 mJ/3–5 ns) with a wavelength range of 420–2300 nm (NT-342B, Ekspla), as reported before [40].

Irradiation for singlet oxygen quantum yield was performed using a general electric quartz lamp (300 W) as described in the literature [41]. Light intensity was measured with a POWER MAX 5100 (Molelectron detector incorporated) power meter and was found to be 4.3×10^{15} photons cm⁻² s⁻¹.

Magnetic circular dichroism (MCD) spectra were measured with a Chirascan plus spectrodichrometer equipped with a 1 T (tesla) permanent magnet by using both the parallel and antiparallel fields. The conventions of Piepho and Schatz are used to describe the sign of the MCD signal and the Faraday terms [42].

X-ray photoelectron spectroscopy (XPS) analysis was done using an AXIS Ultra DLD, with Al (monochromatic) anode equipped with a charge neutraliser, supplied by Kratos Analytical. The following parameters were used: the emission was 10 mA, the anode (HT) was 15 kV and the operating pressure was below 5×10^{-9} Torr. A hybrid lens was used and resolution to acquire scans was at 160 eV pass energy in slot mode. The center used for the scans was at 520 eV with a width of 1205 eV, steps at 1 eV and dwell time at 100 ms as. The high-resolution scans were acquired using 80 eV pass energy in slot mode.

Irradiation for PDT studies was performed using a Modulight Medical (ML) 7710–680 channel Turnkey laser system coupled with a 2 × 3 W channel at 680 nm, cylindrical output channels, aiming beam, integrated calibration module, foot/hand switch pedal, fiber sensors (subminiature version A) connectors and safety interlocks. Illumination kit for *in vitro* PDT studies with capacity to hold 127.76 × 85.48 mm 96 well tissue culture plate.

The MCF-7 cells were cultured in 75 cm² vented flasks (Porvair) in a humidified atmosphere incubator with ~5% CO₂ and temperature at 37 °C (Heal Force). The cells were viewed under phase contrast using a Zeiss® AxioVert.A1 Fluorescence LED (FL-LED) inverted microscope and the cell viability was measured using WST-1 cell proliferation neutral red reagent (Roche) with Synergy 2 multi-mode microplate reader (BioTek®).

2.3. Syntheses

2.3.1. Synthesis of Tris-[(2,2,7,7-tetramethyltetrahydro-3aH-bis([1,3]dioxolo) [4,5-b:4',5'-d]Pyran-5-yl)methoxy]-2-(4-benzo[d]thiazol-2-ylphenoxy Phthalocyaninato) Zinc (II) (**3**)

A mixture of 4-glycosylated phthalonitrile (**1**) (0.55 g, 1.42 mmol), 4-(4-(benzo thiazol-2-yl)phenoxy) phthalonitrile (**2**) (0.1 g, 0.28 mmol), zinc(II) acetate dihydrate (0.25 g, 1.1 mmol) and DBU (0.3 mL), was dissolved in dry 1-pentanol (3 mL). The reaction mixture was refluxed at 180 °C with constant stirring, in the presence of nitrogen for 6 h. The mixture was cooled to ambient temperature and successively precipitated out of solution using methanol. Compound **3** was obtained using silica packed column chromatography with THF:methanol (9:1) as an eluent.

Yield: 0.11 g (16.9%). IR [ν_{\max} /cm⁻¹]: 3196, 2921 (C–H stretch), 1710, 1605 (C=C), 1474–1371 (C=C), 1217 (Ar–O–Ar). UV/Vis (DMSO), λ_{\max} nm (log ε): 682 (5.55), 612 (4.52), 320 (4.78). ¹H NMR (400 MHz, CDCl₃) δ 8.13 (d, *J* = 8.7 Hz, 2H), 8.02 (d, *J* = 8.1 Hz, 1H), 7.87 (d, *J* = 7.8 Hz, 1H), 7.71 (d, *J* = 8.7 Hz, 1H), 7.64 (d, *J* = 8.8 Hz, 2H), 7.52–7.41 (m, 1H), 7.39–7.29 (m, 3H), 7.25 (dd, *J* = 8.9, 2.5 Hz, 3H), 7.16 (dd, *J* = 10.8, 5.7 Hz, 6H), 5.50 (d, *J* = 5.0 Hz, 6H), 4.61 (dd, *J* = 7.9, 2.5 Hz, 6H), 4.33–4.09 (m, 9H), 1.44 (m, 24H), 1.29 (s, 12H).

Anal. Calc. for (C₈₁H₇₇N₉O₁₉SZn): C, 61.65; H, 4.92; N, 7.99; S, 2.03. Found: C, 62.02; H, 5.09; N, 7.02; S, 1.92. MS (MALDI-TOF) *m/z*: Calcd: 1577.97; Found: 1578.44 [M + H]⁺.

2.3.2. Linkage of Complex 3 to AuNPs (AuNS and AuNR; Scheme 2)

Cetyltrimethylammonium bromide (CTAB) stabilized AuNR and AuNS [32,33] were synthesized as reported in literature. Complex **3** is expected to form nitrogen-gold or sulphur-gold bonds through self-assembly mono layers since the benzothiazole portion of the Pc contains sulphur and nitrogen groups. A solution of complex **3** (0.02 g, 0.0127 mmol) in DMSO (3 mL) was mixed with the gold nanoparticles solution, AuNS (0.01 g) in toluene (2 mL) and AuNR (10 mL) in water and stirred for 24 h at room temperature. The conjugates obtained, **3**-AuNS and **3**-AuNR were centrifuged, successively purified with ethanol and allowed to dry in the fume hood.

2.4. Photophysical Studies

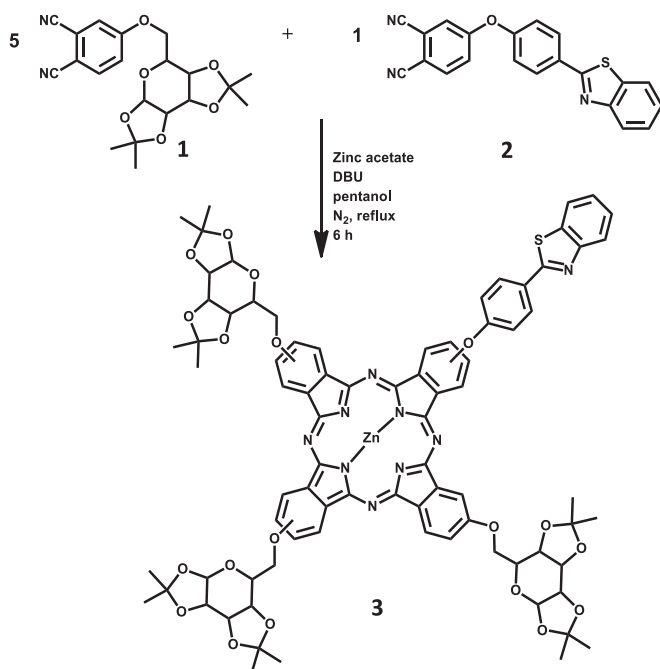
Fluorescence (Φ_F) and triplet (Φ_T) quantum yields of complex **3** and the conjugates were determined in DMSO using comparative methods described before in the literatures [43–45]. Unsubstituted ZnPc in DMSO was used as a standard with $\Phi_F = 0.20$ [44] and $\Phi_T = 0.65$ [45]. The solutions for triplet state studies were de-aerated with argon for 15 min before measurements.

Singlet oxygen quantum yield (Φ_{Δ}) values were determined under ambient conditions using DPBF as a singlet oxygen quencher in DMSO (and ADMA in water) and equations described before [46,47]. ZnPc in DMSO was used as a standard ($\Phi_{\Delta(\text{Std})} = 0.67$ in DMSO) [46]. AlPcSmix was employed as a standard in aqueous media ($\Phi_{\Delta(\text{Std})} = 0.42$ [48]). The absorbances of DPBF or ADMA were spectroscopically monitored at 417 nm or 380 nm, respectively, at predetermined time intervals.

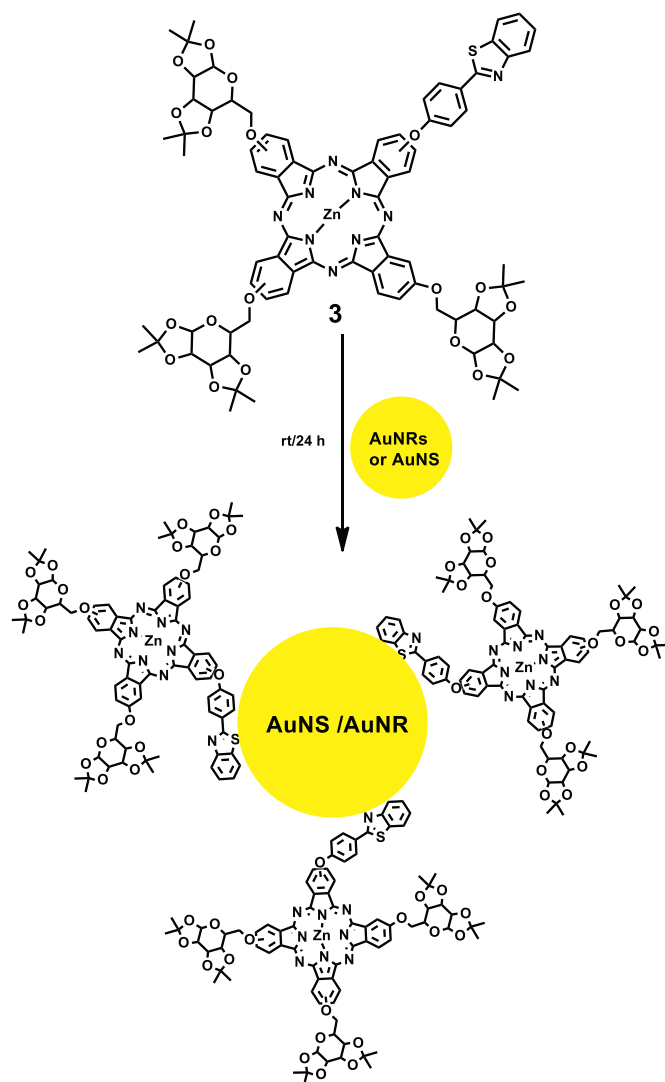
3. Results and Discussion

3.1. Characterization of Complexes 3 and the Conjugates

Schemes 1 and 2, show synthetic pathways for complex **3** and its conjugates with AuNPs. Complex **3** was synthesized through cross-



Scheme 1. Synthesis of complex **3**.



Scheme 2. Illustration of Synthetic pathways for **3**-AuNS and **3**-AuNR.

condensation of phthalonitriles **1** and **2** in the presence of DBU, zinc acetate, and pentanol in an inert nitrogen atmosphere. The disappearance of C≡N peak at 2234 cm⁻¹ (using phthalonitrile **2** as an example) observed for **1** and **2** in the FT-IR spectra (Fig. 1) of **3** confirmed the formation of the latter.

The ¹H NMR spectrum of **3** contains aromatic ring proton peaks between 8.13 and 7.16 ppm. The propylene glycol ring protons were observed between 5.50 and 4.09 ppm, while the CH₃ protons on the sugar were observed between 1.47 and 1.29 ppm (Fig. S1, ESI[†]). Peak integration gave the anticipated total number of protons, confirming the relative purity of the complex. Mass spectral data (Fig. S2, ESI[†]) and elemental analyses agreed with the proposed structure of complex **3**.

3.1.1. Electronic Absorption Spectra

The absorption (solid line) and MCD (dotted line) spectra of complex **3** are shown in Fig. 2. A single Q band at 681 nm was observed for **3**, typical for metalated phthalocyanine with degenerate D_{4h} symmetry [49]. MCD has proven to be a very important technique for identifying the state degeneracies of highly symmetric complexes such as phthalocyanines, because it provides information that cannot be derived from the UV-visible absorption spectrum alone [49]. The MCD spectrum of complex **3** showed a distinct S-shaped sigmoid curve between 600 and 750 nm with a cross-over point at 682 nm, which essentially corresponds to 681 nm wavelength of the absorption maxima. It

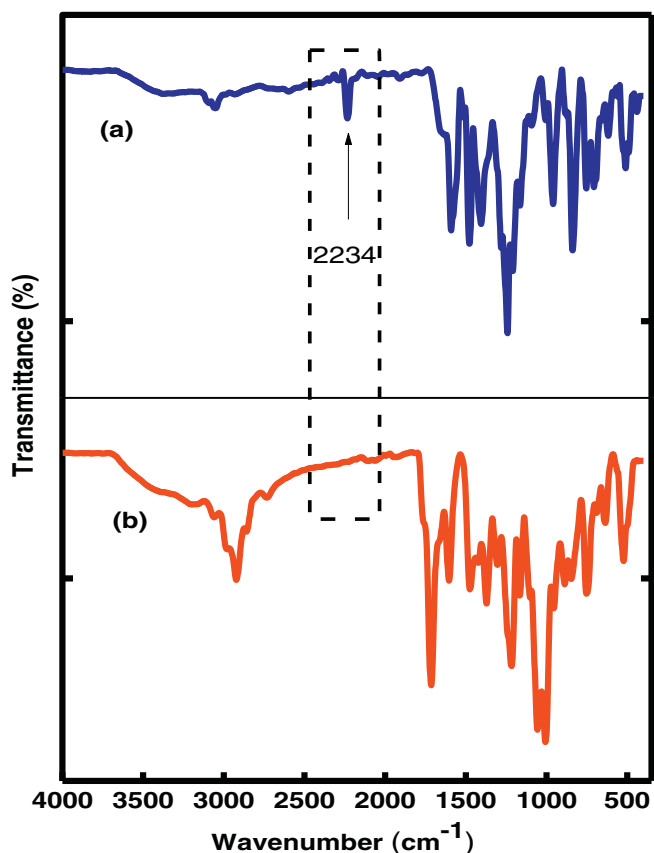


Fig. 1. FTIR spectra of complex 2 (a) and complex 3 (b).

can therefore be assumed that the MCD spectrum in this spectral region is dominated by a pseudo- A_1 term and hence the transition involves a

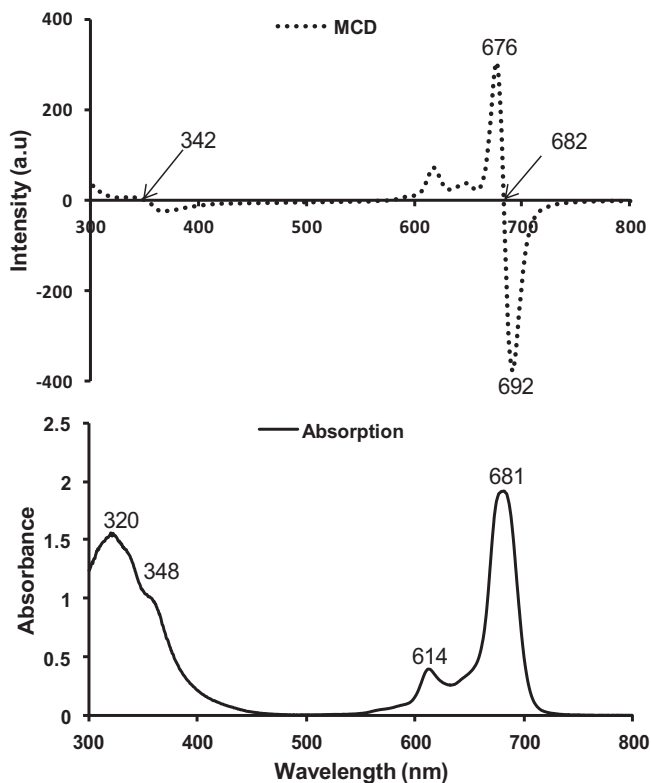


Fig. 2. UV-vis absorption and MCD spectra of complex 3 in DMSO.

near degenerate excited state. A similar curve is also observed in the MCD spectrum at approximately 342 nm, indicating that this transition is also degenerate [50]. From the MCD spectroscopy, the 681 nm and 348 nm bands can be readily assigned as the Q and B bands, respectively in accordance with the Gourterman four-orbital model [51].

The UV-Visible absorption spectra of the gold nanoparticles alone, complex 3 and the conjugates (3-AuNS and 3-AuNR) are shown in Fig. 3. The surface plasmon resonance (SPR) band of the gold nanoparticles (AuNS) was observed at 525 nm (Fig. 3A(a)), characteristic of AuNPs <50 nm [52,53]. On the other hand, gold nanorods (AuNR), Fig. 3B(a), displayed two SPR bands at 519 nm and 662 nm, due to the anisotropic shape corresponding to their width and length known as the transverse and longitudinal modes, respectively [54].

Fig. 3A shows the normalized absorption spectra of AuNS, complex 3 and 3-AuNS in DMSO. Upon conjugation of complex 3 to AuNS, a red-

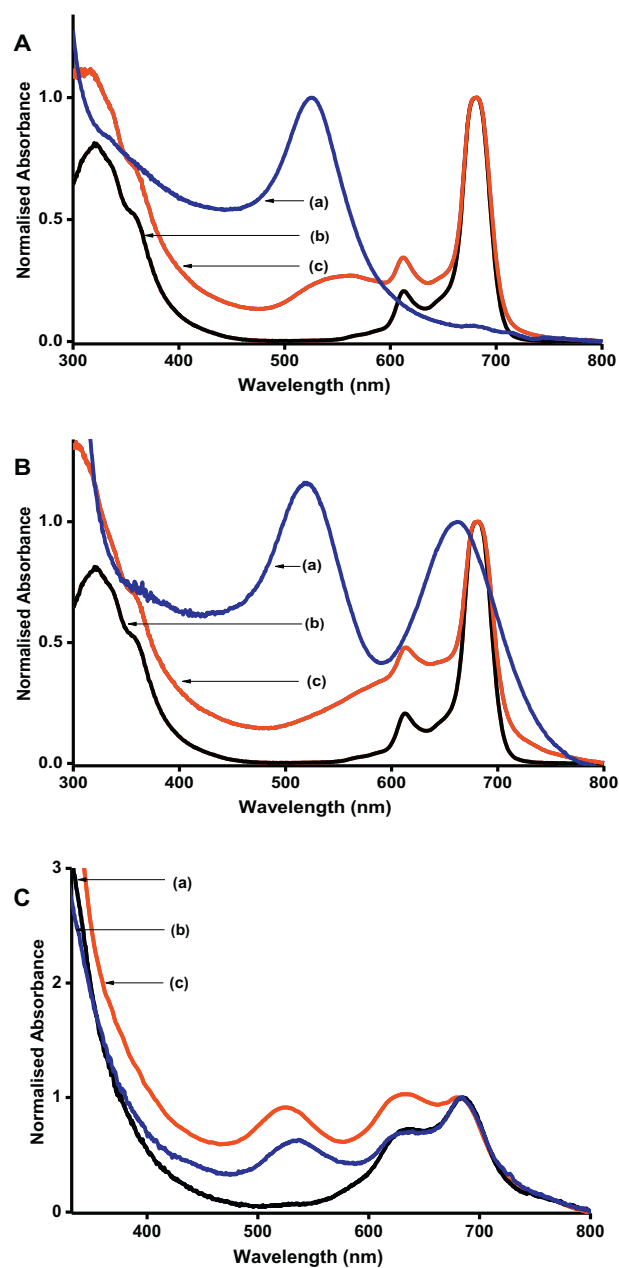


Fig. 3. Absorption spectra of (A) AuNS (a), complex 3 (b), and 3-AuNS (c) in DMSO, (B) AuNR (a), complex 3 (b), and 3-AuNR (c) in DMSO, and (C) complex 3 (a), 3-AuNS (b), 3-AuNR (c) in water.

Table 1Photophysical parameters of complexes **3** and its conjugates in DMSO unless otherwise stated. (Excitation at 609 nm).

Samples	Size ^a	λ_{abs} (nm) ^b	Pc loading ($\mu\text{g}/\text{mg}$)	$\Phi_{\text{F}}(\pm 0.01)$	$\tau_{\text{F}}(\text{ns})(\pm 0.01)$	$\Phi_{\text{T}}(\pm 0.02)$ (DMSO)	$\tau_{\text{T}}(\mu\text{s})(\pm 1.00)$	$\Phi_{\Delta}^{\text{c}}(\pm 0.01)$
3	–	681	–	0.15	2.95	0.51	308	0.36(0.08)
3 -AuNS	15.28 (13.36)	681 (525)	7.62	0.12	2.81	0.62	318	0.55(0.16)
3 -AuNR	3.2 (2.1)	682 (519,662)	13.7	0.11	<0.01	0.71	210	0.61(0.20)

^a Numbers in brackets are the sizes in nm for AuNS alone or aspect ratio of the AuNR alone, all from TEM.^b Numbers in brackets are for the nanoparticles alone in DMSO.^c Numbers in brackets are the values in water.

shift in the SPR was observed from 525 nm to 562 nm indicating an increase in size following conjugation probably due to aggregation. Fig. 3B shows the normalized absorption spectra of AuNR, complex **3** and **3**-AuNR (in DMSO). After conjugation, the presence of AuNR was evidenced by the enhancement in the region where the transverse and longitudinal SPR bands are expected. The latter is masked by the Q band of complex **3** in **3**-AuNR. The spectral enhancement or presence of SPR peaks in the conjugates confirms successful linkage of the complex to nanoparticles.

A potential photosensitizer for photodynamic therapy application should possess relative solubility in aqueous solvent. Fig. 3C shows the absorption spectra of complex **3** and the conjugates in water. These generally show broad Q-bands due to aggregation, typical of Pcs in aqueous solution due to π - π stacking interaction of the aromatic rings of Pcs [55]. The loading of complexes **3** onto the nanoparticles was investigated following literature methods [56]. This involves comparing the Q band absorbance intensity of the Pc in the conjugate with that of the initial Pc before the conjugation. The values are listed in Table 1. Anisotropic nanoparticles have a large surface area [32], which enables the loading of more Pcs.

The ground state absorption, excitation and emission spectra are shown in Fig. 4 (using complex **3** as an example) in DMSO. The ground state absorption and excitation were mirror images of the emission spectrum. The closeness of the Q-band absorption maxima to that of excitation shows that the ground state nuclear configuration of complex **3** was not affected by excitation and that there is no aggregation.

3.1.2. XRD Studies

Fig. 5 shows the X-ray diffraction (XRD) pattern for AuNS, complex **3**, **3**-AuNS and **3**-AuNR. The XRD diffraction patterns of the nanoparticles (Fig. 5A) showed well-defined crystalline peaks assigned to the planes at 111, 200, 220, 311 and 222 corresponding to the face centered-cubic structures of metallic gold [57]. The XRD pattern of complex **3** contains sharp peaks between $2\theta = 18$ – 23° . Sharp XRD peaks are

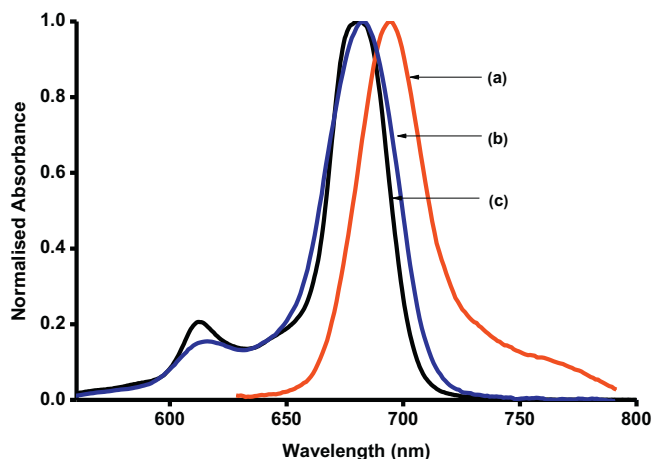


Fig. 4. Emission (a), excitation (b) and absorption (c) spectra of complex **3** (excitation = 609 nm, solvent = DMSO).

not unusual in the XRD patterns of phthalocyanines [58]. The XRD diffractogram for the conjugates of phthalocyanines (Pcs) and AuNPs depicted the disappearance (or reduction in the number) of crystalline peaks at $2\theta = 10$ – 30° seen in Pcs alone with slight broadening possibly due to interaction between the Pcs and AuNPs [59] in addition to the gold peaks, (Fig. 5B and C) confirming the formation of **3**-AuNS and **3**-AuNR.

Debye-Scherrer Eq. (1) [60] was employed for the estimation of the sizes of the AuNS:

$$d = \frac{k\lambda}{\beta \cos\theta} \quad (1)$$

where λ is the wavelength of the X-ray source (1.5405 Å), k is an empirical constant equal to 0.9, β is the full width at half maximum of the diffraction peak and θ is the angular position. The sizes were estimated to be 12.0 nm (AuNS) and 14.6 nm (**3**-AuNS).

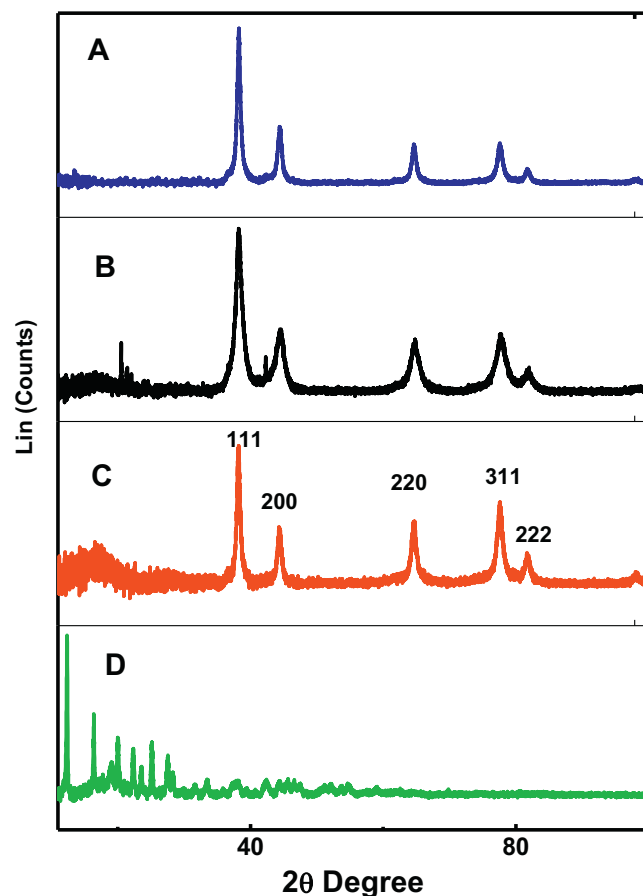


Fig. 5. XRD diffractograms for AuNS (A), **3**-AuNS (B), **3**-AuNR, and (C) complex **3** (D).

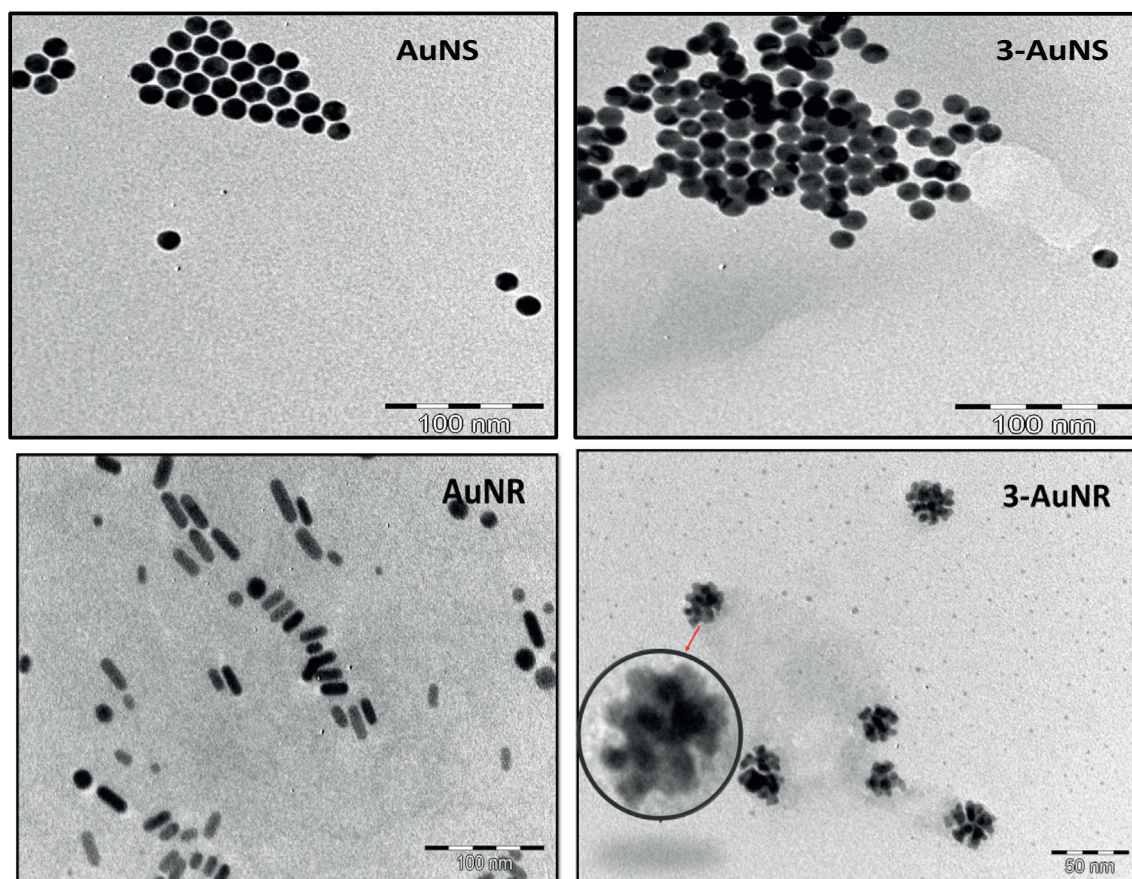


Fig. 6. Representative TEM micrographs for AuNS, AuNR and when conjugated to complex **3**.

3.1.3. TEM

The TEM micrographs for AuNS, AuNR, **3**-AuNS and **3**-AuNR are shown in Fig. 6. The AuNS were spherical and relatively monodispersed. The TEM micrograph for AuNR clearly shows rods. Upon conjugation, both **3**-AuNS and **3**-AuNR showed aggregation, with the nanorods in **3**-AuNR intertwined as shown in the zoomed insert in the TEM micrograph for **3**-AuNR. The presence of the NRs in the conjugates is clear showing their integrity. Aggregation is probably due to interactions between the Pcs on adjacent NPs via π - π stacking since Pcs are known for their π - π stacking to form H aggregates [55]. The sizes were 13.36 nm (AuNS), 15.28 nm (**3**-AuNS), and the aspect ratio 2.1 (AuNR) and 3.2 (**3**-AuNR), Table 1. There is an increase in size following conjugation as was the case for XRD.

3.1.4. EDX Spectra

The elemental composition of the NPs, complexes and their conjugates were qualitatively determined by energy dispersive X-ray spectrometer (EDX), Fig. 7. The spectrum of complex **3**, showed the presence of C, N, S, O and Zn, as expected for the phthalocyanine. Upon conjugation to the gold nanoparticles, the spectrum (Fig. 7B and C) displayed a Au peak in addition to elements seen in the complex alone. Fig. 7C shows the presence of silver from silver nitrate that was used during the preparation of the growth solution for the synthesis of AuNR.

3.1.5. XPS Spectra

An assessment of the possible interaction between AuNPs and complex **3** was done using XPS analysis. The XPS survey spectra (Fig. 8A) exhibited the expected elements and their respective binding energies. Complex **3** exhibited S (163 eV), C (285 eV), N (397 eV), O (534 eV),

and Zn (1026 eV), while its conjugates (**3**-AuNR and **3**-AuNS) displayed similar trends but with an additional atom, Au (85.21 eV, 338 eV and 353 eV).

The high resolution XPS analysis was employed to show the possible linkage of complex **3** to AuNPs. The N 1s peak for complex **3** alone (Fig. 8B) showed two subpeaks corresponding to —N—C— (396.2 eV) and —N— (397.3 eV), while the conjugates (Fig. 8C, **3**-AuNS as an example) displayed three peaks attributed to —N—C— (396.3 eV), —N— (397.3 eV) and —N—Au— (399.9 eV). The S 2p deconvolution for complex **3** alone (Fig. 8D) exhibited two subpeaks corresponding to —S—C— (161.9 eV) and —S— (163.1 eV). The conjugates (Fig. 8E, **3**-AuNS as an example) displayed three peaks attributed to —S—C— (161.8 eV), —S— (163.8 eV) and —S—Au— (164.5 eV). The presence of the gold to sulphur and gold to nitrogen interaction (—N—Au— and —S—Au—) suggests that either both S and N on the same Pc molecule are linked to AuNPs or that some molecules of **3** were adsorbed on the surface of metallic nanoparticles through S—Au interactions while others utilized the N—Au interactions since gold has a strong affinity for both sulphur and nitrogen. The N 1s and S 2p spectra for **3**-AuNR, is shown in Fig. S3, ESI[†].

3.2. Photophysicochemical Parameters

3.2.1. Fluorescence Quantum Yields (Φ_F) and Lifetimes (τ_F)

As shown in Table 1, the Φ_F of complex **3** in the presence of AuNPs decreases probably due to deactivation of the excited singlet state through heavy atom effect which promotes intersystem crossing to the triplet state thus lowering the Φ_F [61]. The fluorescence lifetimes also decreased following conjugation as expected since fluorescence quantum yields and lifetimes have a direct relationship. A typical

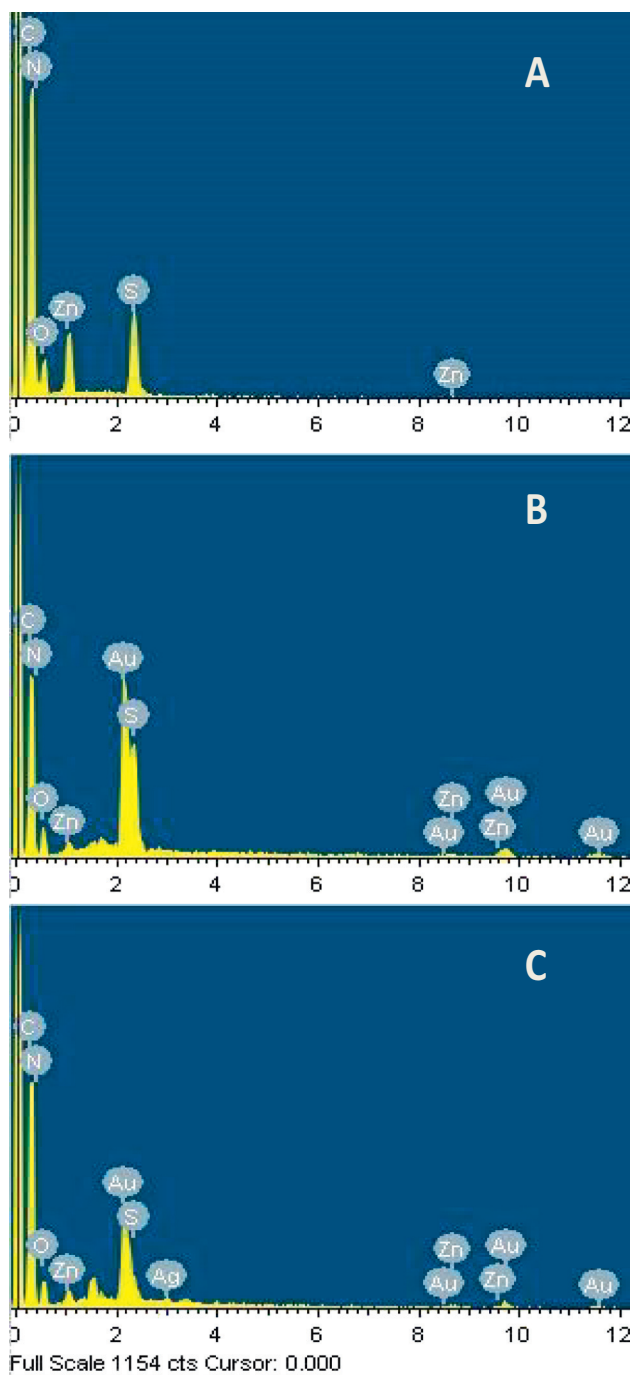


Fig. 7. EDX spectra of complex **3** (A), 3-AuNS (B), and 3-AuNR (C).

fluorescence decay curve for complex **3** (as an example) is as shown in Fig. 9. A mono-exponential decay curve indicating one life-time was obtained for complex **3** alone and conjugates showed two lifetimes. The presence of two life times could be due to different orientations of Pcs on the NPs. Comparing the lifetime of **3** alone with the metallic nanoconjugates, a drastic reduction in lifetime was observed for 3-AuNR while 3-AuNS only showed slight decrease. The metal-enhanced fluorescence and reduction in lifetime of nano hybrids has been shown both theoretically and experimentally to be dependent on the overlap between the fluorescence emission of dye molecule and the surface plasmon resonance (SPR) band of the metallic nanoparticles [62–64].

Li et al. [62] have found that when the wavelength of SPR band in metallic nanoparticles are far apart from that of the fluorescence

emission of dye molecules, the reduction in lifetime of the resultant nano hybrid is not significant, but a drastic reduction in lifetime was observed when the wavelength is close or overlap. This is because absorption in metallic nanoparticles opens loss channels and shortens the fluorescence lifetime at very close distances, leading to quenching [62,64]. From Fig. S4, ESI[†], it can be clearly seen that complex **3** emission maxima almost overlap with that of the absorption of AuNR but far apart with the AuNS, hence a drastic reduction in lifetime for 3-AuNR compared to 3-AuNS.

3.2.2. Triplet Quantum Yields (Φ_T) and Lifetimes (τ_T)

The triplet decay curve of 3-AuNR is shown in Fig. 10 (as an example) and all the Pcs and conjugates were found to obey second order kinetics, which is typical of MPcs complexes at high concentration, due to triplet-triplet recombination [65]. The increase in triplet quantum yield observed upon conjugation (Table 1), corresponding to the decrease in fluorescence quantum yield, showed that AuNPs promote intersystem crossing to the triplet state due to heavy atom effect as mentioned

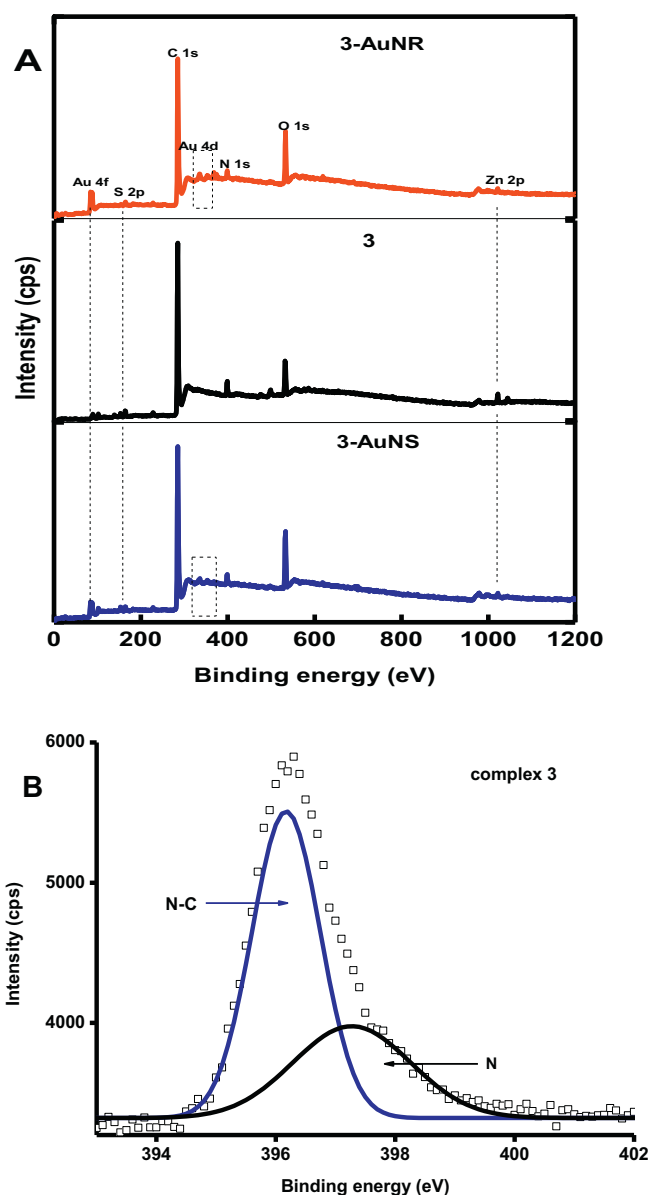


Fig. 8. XPS spectra: (A) survey spectra of complex **3**, 3-AuNS, 3-AuNR and high resolution spectra (B) N 1s for complex **3**, (C) N 1s for 3-AuNS, (D) S 2p for complex **3**, and (E) S 2p for 3-AuNS.

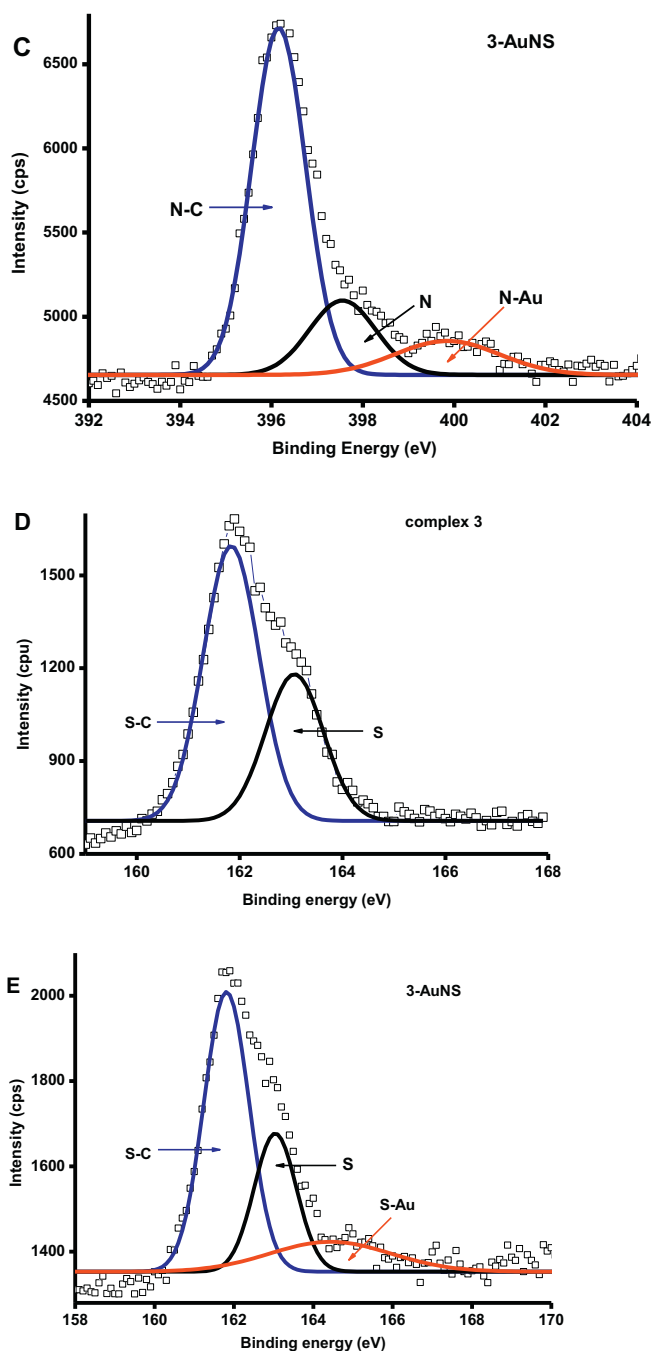
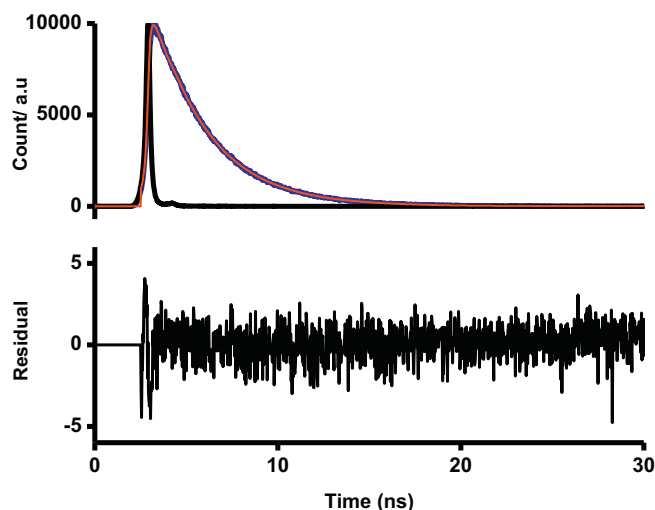


Fig. 8 (continued).

above. The conjugate 3-AuNR gave larger Φ_T values compared to 3-AuNS (Table 1). 3-AuNR with a higher loading gave a high Φ_T than 3-AuNS.

Additionally, the longitudinal SPR peak of the nanorod at 686 nm which overlaps with the Q band of 3 at 681 nm could be having an effect on the excited state parameters. The residual silver ion (see Fig. 7C) used in the synthesis of AuNR could also be contributing through the heavy atom effect.

There was a decrease in triplet lifetimes for complex 3 in the presence of AuNR due to the presence of Au, a heavy metal, corresponding to an increase in Φ_T as expected. However, for complex 3 in the presence of AuNS there was a lengthening of triplet lifetimes. Lengthening of triplet lifetimes of Pcs in the presence of nanoparticles has been observed before [66] and was attributed to the protection of the Pc by

Fig. 9. Fluorescence decay (blue), χ^2 fitting (red) and IRF (black) curves for complex 3 in DMSO.

the nanoparticles. The Φ_T in water could not be determined since water quenches the triplet state.

3.2.3. Singlet Oxygen Quantum Yields

Singlet oxygen is produced when the excited triplet state photosensitizer transfers its energy to ground state molecular oxygen. Thus, singlet oxygen quantum yield (Φ_Δ) is a measure of the efficiency of the processes resulting in the generation of singlet oxygen. To determine the singlet oxygen quantum yield (Φ_Δ), the chemical photodegradation of the singlet oxygen quencher (DPBF) in DMSO (using complex 3) and (ADMA) in water (using 3-AuNR) was monitored over a period of time (Fig. 11). The Q-band of complex 3 remained unchanged, proving the stability of the complex over the irradiation period, while DPBF and ADMA degraded. A significant increase in singlet oxygen generation was observed as evidenced by singlet oxygen quantum yield (Table 1) upon conjugation of complex 3 to gold nanoparticles corresponding to an increase in triplet quantum yield. Values are low in water due to aggregation. In addition, water is known to quench the singlet state [44]. The enhancement observed in 3-AuNR compared to 3-AuNS could also be due to the advantage of asymmetry in 3-AuNR. The

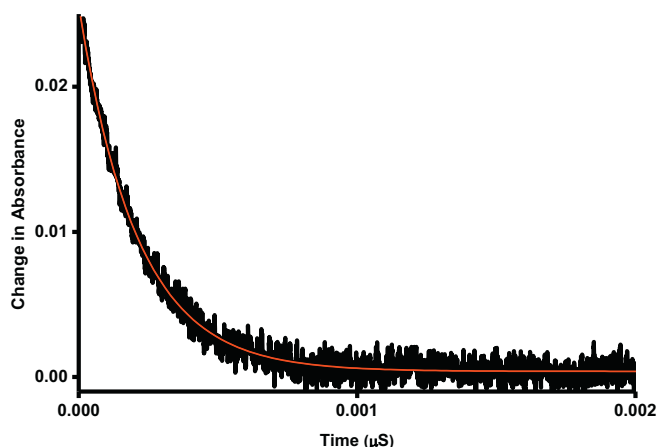


Fig. 10. Triplet absorption decay curve (black) and fitting (red) for 3-AuNS in DMSO.

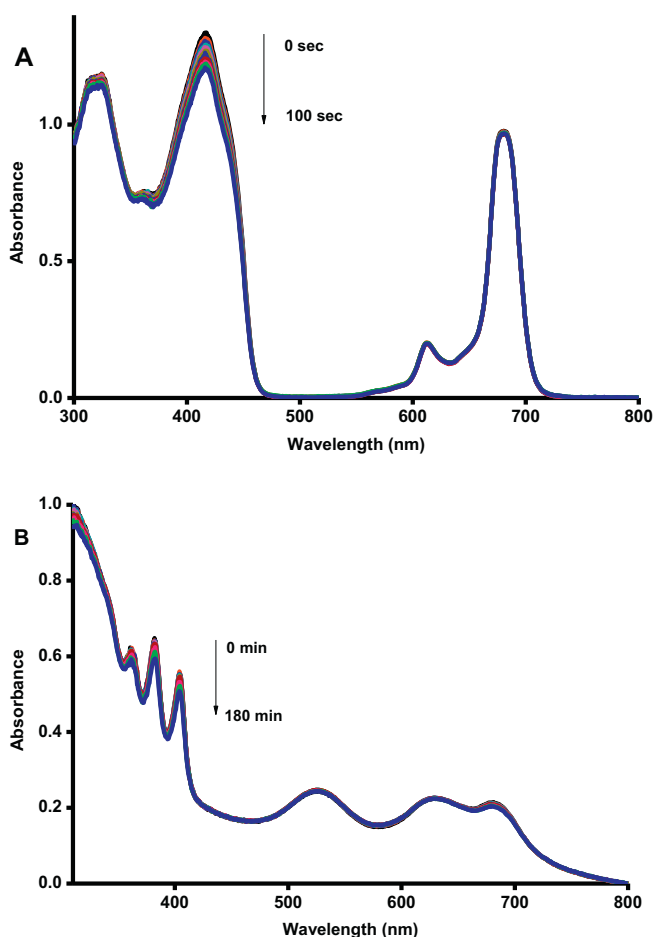


Fig. 11. Representative spectra for singlet oxygen quantum yield determination using a photochemical method. The spectra show the degradation of (A) DPBF in the presence of complex 3 in DMSO and (B) ADMA in the presence of 3-AuNR.

enhancement of the singlet oxygen quantum yield on conjugation shows that this complex may be used for photodynamic therapy in the presence of different shapes of AuNPs.

3.3. Cell Studies

The *in vitro* dark cytotoxicity and photodynamic therapy was carried out as reported in the literature [67].

In vitro dark cytotoxicity and photodynamic therapy of complex 3 and its conjugates with both AuNR and AuNS were tested against MCF-7 cells. The vehicle control (1.6% DMSO in culture media being the highest concentration of DMSO used for all photosensitizers used in this study) was equally tested against MCF-7 cells to assess the effects of solvent against the cells. The percentage cell viability of the 1.6% DMSO was relatively the same as the media control alone. Gradient photosensitizer concentration range of 10 $\mu\text{g/mL}$ to 160 $\mu\text{g/mL}$ for *in vitro* dark cytotoxicity and PDT were used. A fixed light dosimetry of 170 $\text{J}\cdot\text{cm}^2$ was used for the PDT studies.

3.3.1. In Vitro Dark Cytotoxicity

Complex 3 and its conjugates (3-AuNR and 3-AuNS) accounted for $\geq 85\%$ viable cells at concentration $\leq 160 \mu\text{g/mL}$ which further lay credence to the innocuous behaviour of phthalocyanine when in dark without light activation. Dark cytotoxicity is not desirable in PDT applications as it can result in cytotoxic activity against both the healthy and unhealthy (cancerous) cells. The AuNR alone (Fig. S5, ESI[†]) showed slight dark toxicity, with $\geq 81\%$ viable cells at concentration $\leq 160 \mu\text{g/mL}$,

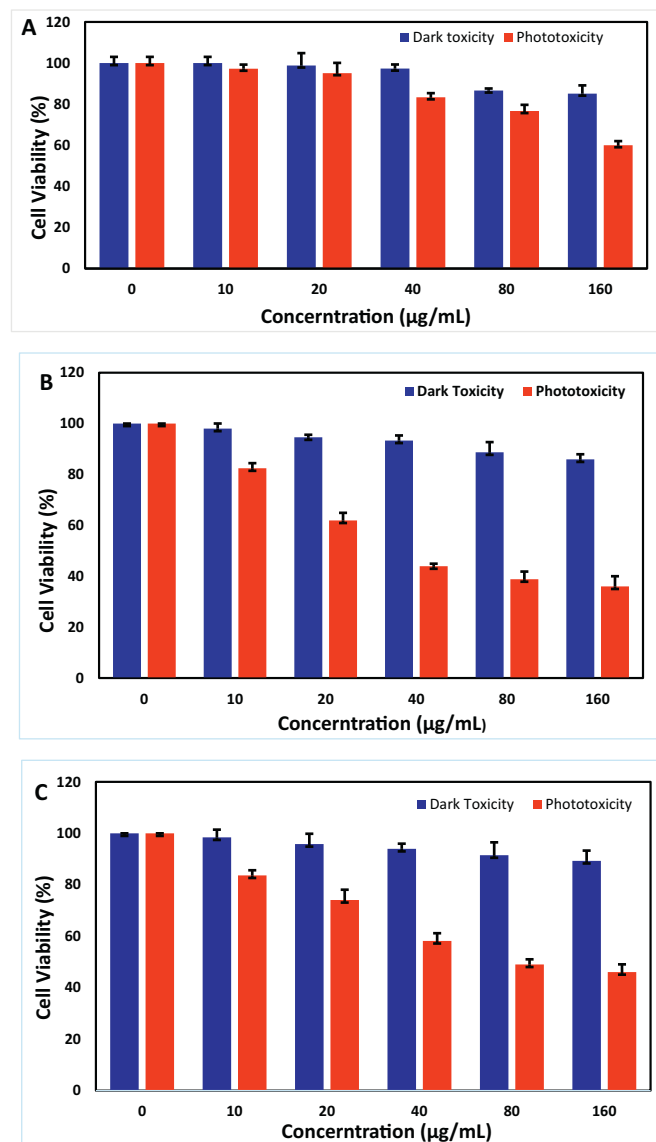


Fig. 12. Dark toxicity and phototoxicity effects of complex 3 (A), 3-AuNR (B) and 3-AuNS (C) against epithelial breast cancer cells (MCF-7). Fixed irradiation dose = 170 $\text{J}\cdot\text{cm}^2$.

and this was attributed to the CTAB adsorbed on the surfaces of the nanorods. The toxicity of the CTAB-capped nanorod has been reported before [68–73] and has been attributed to residual CTAB on the surfaces of the rods and not the rods themselves. It is noteworthy that the presence of Pcs in the conjugate decrease the dark cytotoxicity observed in the CTAB-capped nanorods alone. This suggests that most of the CTAB on the nanorods were replaced by the Pc on conjugation.

3.3.2. Photodynamic Therapy Activity

As earlier stated, a fixed light dosimetry of 170 $\text{J}\cdot\text{cm}^2$ and gradient photosensitizer concentration range of 10 $\mu\text{g/mL}$ to 160 $\mu\text{g/mL}$ were used against the MCF-7 cells. Complex 3 alone (Fig. 12A) showed cell viability $> 50\%$ at concentrations $\leq 160 \mu\text{g/mL}$. This could be attributed to aggregation in aqueous media, which leads to lower singlet oxygen generation ($\Phi_{\Delta} = 0.08$). The nanoparticles alone (Fig. S5, ESI[†]) displayed phototoxicity attributed to the photothermal activity of gold, known to be a light absorber for cancer therapy [74,75]. The conjugate, 3-AuNR (Fig. 12B) afforded superior PDT activity with $< 50\%$ viable cells at concentrations $\geq 40 \mu\text{g/mL}$ in comparison with 3-AuNS (Fig. 12C) with $< 50\%$ viable cells at concentrations $\geq 80 \mu\text{g/mL}$. The superior PDT

activity of **3**-AuNR compared to **3**-AuNS is attributed to the higher singlet oxygen quantum yield (Table 1), in addition to enhanced photothermal activity due to the presence of nanorods. It should be noted that for the PDT studies, excitation was performed at 680 nm and AuNR (with SPR bands at 519 nm and 662 nm) absorb more light at this wavelength than AuNS (with SPR bands at 525 nm). The enhanced PDT activity for the conjugates compared to complex **3** alone is attributed to the advantage of photothermal therapy in addition to the enhanced singlet oxygen quantum yield of the conjugates as shown in Table 1, due to the presence of Au, a heavy atom and light absorber, as explained before.

4. Conclusion

Tris-[(2,2,7,7-tetramethyltetrahydro-3aH-bis([1,3]dioxolo)[4,5-b:4',5'-d]pyran-5-yl) methoxy)-2-(4-benzo[d]thiazol-2-yl)phenoxyphthalocyaninato] zinc(II) (complex **3**) was synthesized and linked to AuNPs through S-Au/N-Au self-assembly. The conjugates displayed improved triplet and singlet quantum yields than complex **3** alone; however, **3**-AuNR performed better than **3**-AuNS. Complex **3** and its conjugates showed less *in vitro* dark cytotoxicity with >85% viable cells in all the tested concentrations. **3**-AuNR with enhanced photothermal therapy showed better PDT activity than **3**-AuNS. The conjugates (**3**-AuNT and **3**-AuNT) have potential for application as PS in PDT for cancer treatment.

Acknowledgements

This work was supported by the Department of Science and Technology (DST) Innovation and National Research Foundation (NRF), South Africa through DST/NRF South African Research Chairs Initiative for Professor of Medicinal Chemistry and Nanotechnology (UID 62620) as well as Rhodes University.

Appendix A. Supplementary Data

Supplementary data to this article can be found online at <https://doi.org/10.1016/j.saa.2018.05.081>.

References

- N.L. Oleinick, R.L. Morris, I. Belichenko, The role of apoptosis in response to photodynamic therapy: what, where, why, and how, *Photochem. Photobiol. Sci.* 1 (2002) 1–21.
- Y. Chen, M. Hanack, Y. Araki, O. Ito, Axially modified gallium phthalocyanines and naphthalocyanines for optical limiting, *Chem. Soc. Rev.* 34 (2005) 517–529.
- H. Ali, J.E. van Lier, Metal complexes as photo- and radio-sensitizers, *Chem. Rev.* 99 (1999) 2379–2450.
- M. Allen, W.M. Sharman, J.E. van Lier, Current status of phthalocyanines in the photodynamic therapy of cancer, *J. Porphyrins Phthalocyanines* 5 (2001) 161–169.
- M. Wainwright, Photodynamic antimicrobial chemotherapy (PACT), *J. Antimicrob. Chemother.* 42 (1998) 13–28.
- A.S. Derycke, P.A. de Witte, Liposomes for photodynamic therapy, *Adv. Drug Deliv. Rev.* 56 (2004) 17–30.
- A.R. Simioni, M.M. Pelisson, M. Beltrame, A.C. Tedesco, Photophysical and photobiological studies of a silicon tribenzonaphthoporphyrin incorporated into liposomes for photodynamic therapy use, *J. Nanosci. Nanotechnol.* 8 (2008) 3208–3215.
- K. Sugisaki, T. Usui, N. Nishiyama, W.D. Jang, Y. Yanagi, S. Yamagami, S. Amano, K. Kataoka, Photodynamic therapy for corneal neovascularization using polymeric micelles encapsulating dendrimer porphyrins, *Invest. Ophthalmol. Vis. Sci.* 49 (2008) 894–899.
- C.F. van Nostrum, Polymeric micelles to deliver photosensitizers for photodynamic therapy, *Adv. Drug Deliv. Rev.* 56 (2004) 9–16.
- M. Bhatti, G. Yahioğlu, L.R. Milgrom, M. Garcia-Maya, K.A. Chester, M.P. Deonarain, Targeted photodynamic therapy with multiply-loaded recombinant antibody fragments, *Int. J. Cancer* 122 (2008) 1155–1163.
- C. Staneloudi, K.A. Smith, R. Hudson, N. Malatesti, H. Savoie, R.W. Boyle, J. Greenman, Development and characterization of novel photosensitizer: scFv conjugates for use in photodynamic therapy of cancer, *Immunology* 120 (2007) 512–517.
- S. De Luca, D. Tesaro, P. Di Lello, R. Fattorusso, M. Saviano, C. Pedone, G. Morelli, Synthesis and solution characterization of a porphyrin-CCK8 conjugate, *J. Pept. Sci.* 7 (2001) 386–394.
- K. Ichikawa, T. Hikita, N. Maeda, S. Yonezawa, Y. Takeuchi, T. Asai, Y. Namba, N. Oku, Antiangiogenic photodynamic therapy (PDT) by using long-circulating liposomes modified with peptide specific to angiogenic vessels, *Biochim. Biophys. Acta* 1669 (2005) 69–74.
- C.L. Conway, I. Walker, A. Bell, D.J. Roberts, S.B. Brown, D.I. Vernon, In vivo and in vitro characterisation of a protoporphyrin IX-cyclic RGD peptide conjugate for use in photodynamic therapy, *Photochem. Photobiol. Sci.* 7 (2008) 290–298.
- I. Roy, T.Y. Ohulchanskyy, H.E. Pudavar, E.J. Bergey, A.R. Oseroff, J. Morgan, T.J. Dougherty, P.N. Prasad, Ceramic-based nanoparticles entrapping water-insoluble photosensitizing anticancer drugs: a novel drug-carrier system for photodynamic therapy, *J. Am. Chem. Soc.* 125 (2003) 7860–7865.
- M.E. Wieder, D.C. Hone, M.J. Cook, M.M. Handsley, J. Gavrilovic, D.A. Russell, Intracellular photodynamic therapy with photosensitizer-nanoparticle conjugates: cancer therapy using a 'Trojan horse', *Photochem. Photobiol. Sci.* 5 (2006) 727–734.
- Z. Iqbal, A. Lyubimtsev, M. Hanack, T. Ziegler, Anomerically glycosylated zinc(II) naphthalocyanines, *Tetrahedron Lett.* 50 (2009) 5681–5685.
- I. Laville, S. Pigaglio, J.C. Blais, F. Doz, B. Looock, P. Maillard, D.S. Grierson, J. Blais, Photodynamic efficiency of diethylene glycol-linked glycoconjugated porphyrins in human retinoblastoma cells, *J. Med. Chem.* 49 (2006) 2558–2567.
- P.C. Lo, C.M. Chan, J.Y. Liu, W.P. Fong, D.K. Ng, Highly photocytotoxic glycosylated silicon(IV) phthalocyanines. Effects of peripheral chloro substitution on the photophysical and photodynamic properties, *J. Med. Chem.* 50 (2007) 2100–2107.
- Y. Zorlu, M.A. Ermeşyan, F. Dumoulin, V. Ahsen, H. Savoie, R.W. Boyle, Glycerol and galactose substituted zinc phthalocyanines. Synthesis and photodynamic activity, *Photochem. Photobiol. Sci.* 8 (2009) 312–318.
- C.F. Choi, J.D. Huang, P.C. Lo, W.P. Fong, D.K. Ng, Glycosylated zinc(II) phthalocyanines as efficient photosensitizers for photodynamic therapy. Synthesis, photophysical properties and in vitro photodynamic activity, *Org. Biomol. Chem.* 6 (2008) 2173–2181.
- S.G. Kimani, T.A. Shmigol, S. Hammond, J.B. Phillips, J.I. Bruce, A.J. MacRobert, M.V. Malakhov, J.P. Golding, Fully protected glycosylated zinc(II) phthalocyanine shows high uptake and photodynamic cytotoxicity in MCF-7 Cancer Cells, *Photochem. Photobiol.* 89 (2013) 139–149.
- R.E. Airley, A. Mobasher, Hypoxic regulation of glucose transport, anaerobic metabolism and angiogenesis in cancer: novel pathways and targets for anticancer therapeutics, *Chemotherapy* 53 (2007) 233.
- X. Cao, L. Fang, S. Gibbs, Y. Huang, Z. Dai, P. Wen, X. Zheng, W. Sadee, D. Sun, Glucose uptake inhibitor sensitizes cancer cells to daunorubicin and overcomes drug resistance in hypoxia, *Cancer Chemother. Pharmacol.* 59 (2007) 495–505.
- R. Diaz-Ruiz, M. Rigoulet, A. Devin, The Warburg and Crabtree effects: on the origin of cancer cell energy metabolism and of yeast glucose repression, *Biochim. Biophys. Acta* 1807 (2011) 568–576.
- P. Chen, S. Mwakwari, A. Oyelere, Gold nanoparticles: from nanomedicine to nanosensing, *Nanotechnology* 1 (2008) 45–66.
- Z. Iqbal, M. Hanack, T. Ziegler, Synthesis of an octasubstituted galactose zinc(II) phthalocyanine, *Tetrahedron Lett.* 50 (2009) 873–875.
- M.A. Ermeşyan, F. Dumoulin, T.V. Basova, D. Bouchu, A.G. Gurek, V. Ahsen, D. Lafont, Amphiphilic carbohydrate phthalocyanine conjugates obtained by glycosylation or by azidealkyne click reaction, *New J. Chem.* 34 (2010) 1153–1162.
- M.S. Rodríguez-Morgade, G. de la Torre, T. Torres, Design and synthesis of low symmetry phthalocyanines and related systems, in: K.M. Kadish, K.M. Smith, R. Guilard (Eds.), *Phthalocyanines: Synthesis, the Porphyrin Handbook*, Academic Press, San Diego 2003, pp. 125–160.
- D.A. Horton, G.T. Bourne, M.L. Smythe, The combinatorial synthesis of bicyclic privileged structures or privileged substructures, *Chem. Rev.* 103 (2003) 893–930.
- S.H. Kok, R. Gambari, C.H. Chui, M.C. Yuen, E. Lin, R.S.M. Wong, F.Y. Lau, G.Y. Cheng, W.S. Lam, S.H. Chan, K.H. Lam, C.H. Cheng, P.B.S. Lai, M.W.Y. Yu, F. Cheung, J.C. Tanga, A.S.C. Chan, Synthesis and anti-cancer activity of benzothiazole containing phthalimide on human carcinoma cell lines, *Bioorg. Med. Chem.* 16 (2008) 3626–3631.
- T. Mthethwa, T. Nyokong, Fluorescence behavior and singlet oxygen generating abilities of aluminum phthalocyanine in the presence of anisotropic gold nanoparticles, *J. Lumin.* 157 (2015) 207–214.
- K.A. Kozek, K.M. Kozek, Wei-Chen Wu, S.R. Mishra, J.B. Tracy, Large-scale synthesis of gold nanorods through continuous secondary growth, *Chem. Mater.* 25 (2013) 4537–4544.
- G. van Maltzahn, J. Park, A. Agrawal, N.K. Bandaru, S.K. Das, M.J. Sailor, S.N. Bhatia, Computationally guided photothermal tumor therapy using long-circulating gold nanorod antennas, *Cancer Res.* 69 (2009) 3892–3900.
- J. Park, G. von Maltzahn, L.L. Ong, A. Centrone, T.A. Hatton, E. Ruoslahti, S.N. Bhatia, M.J. Sailor, Cooperative nanoparticles for tumor detection and photothermally triggered drug delivery, *Adv. Mater.* 22 (2010) 880–885.
- N. Nombona, K. Maduray, E. Antunes, A. Karsten, T. Nyokong, Synthesis of phthalocyanine conjugated with gold nanoparticles and liposomes for photodynamic therapy, *J. Photochem. Photobiol. B Biol.* 107 (2012) 35–44.
- M. Ambroz, A. Beeby, A.J. McRobert, M.S.C. Simpson, R.K. Svensen, D. Phillips, Preparative, analytical and fluorescence spectroscopic studies of sulphonated aluminium phthalocyanine photosensitizers, *J. Photochem. Photobiol. B Biol.* 1 (1999) 87–95.
- N. Nwaji, B. Jones, J. Mack, T. Nyokong, Nonlinear optical dynamic of benzothiazole derivatized phthalocyanines in solution, thin film and when conjugated to nanoparticles, *J. Photochem. Photobiol. A Chem.* 346 (2017) 46–59.
- T.P. Mthethwa, S. Tuncel, M. Durmuş, T. Nyokong, Photophysical and photochemical properties of a novel thiol terminated low symmetry zinc phthalocyanine complex and its gold nanoparticles conjugate, *Dalton Trans.* 42 (2013) 4922–4930.
- A. Fashina, E. Antunes, T. Nyokong, Characterization and photophysical behavior of phthalocyanines when grafted onto silica nanoparticles, *Polyhedron* 53 (2013) 278–285.

- [41] N. Masilela, T. Nyokong, The interaction of silver nanoparticles with low symmetry cysteinyl metallophthalocyanines and their antimicrobial effect, *J. Photochem. Photobiol. A Chem.* 255 (2013) 1–9.
- [42] M. Decker, M.W. Klein, M. Wegener, S. Linden, Circular dichroism of planar chiral magnetic metamaterials, *Opt. Lett.* 32 (2007) 856–858.
- [43] S. Fery-Forgues, D. Lavabre, Modified mesoporous silica nanoparticles as a reusable, selective chromogenic sensor for mercury(II) recognition, *J. Chem. Educ.* 76 (1999) 1260–1264.
- [44] A. Ogunsipe, J.Y. Chen, T. Nyokong, Photophysical and photochemical studies of zinc (II) phthalocyanine derivatives—effects of substituents and solvents, *New J. Chem.* 28 (2004) 822–827.
- [45] T.H. Tran-Thi, C. Desforge, C. Thiec, S.J. Gaspard, Singlet–singlet and triplet–triplet intramolecular transfer processes in a covalently linked porphyrin–phthalocyanine heterodimer, *J. Phys. Chem.* 93 (1989) 1226–1233.
- [46] N.A. Kuznetsova, N.S. Gretsova, O.A. Yuzhakova, V.M. Negrinovskii, O.L. Kaliya, E.A. Luk'yanets, New reagents for determination of the quantum efficiency of singlet oxygen generation in aqueous media, *Russ. J. Gen. Chem.* 71 (2001) 36–41.
- [47] W. Spiller, H. Kliensch, D. Wohrle, S. Hackbarth, B. Roder, G. Schnurpfeil, Singlet oxygen quantum yields of different photo-sensitizers in polar solvents and micellar solutions, *J. Porphyrins Phthalocyanines* 2 (1998) 145–158.
- [48] T. Nyokong, E. Antunes, Photochemical and photophysical properties of metallophthalocyanines, in: K.M. Kadish, K.M. Smith, R. Guilard (Eds.), *The Handbook of Porphyrin Science*, World Scientific, Singapore 2010, pp. 247–349.
- [49] J. Mack, M.J. Stillman, in: K.M. Kadish, K.M. Smith, R. Guilard (Eds.), *The Porphyrin Handbook*, Academic Press, New York, 2003.
- [50] J. Mack, M.J. Stillman, N. Kobayashi, Application of MCD spectroscopy to porphyrinoids, *Coord. Chem. Rev.* 251 (2007) 429–453.
- [51] M. Gouterman, *Optical Spectra and Electronic Structure of Porphyrins and Related Rings*, Academic Press, New York, 1978.
- [52] P.K. Jain, I.H. El-Sayed, M.A. El-Sayed, Au nanoparticles target cancer, *NanoToday* 2 (2007) 18–29.
- [53] F. Mafune, Structure diagram of gold nanoparticles in solution under irradiation of UV pulse laser, *Chem. Phys. Lett.* 397 (2004) 133–137.
- [54] S. Ke, C. Kan, J. Liu, B. Cong, Controlled assembly of gold nanorods using tetrahydrofuran, *RSC Adv.* 3 (2013) 2690–2696.
- [55] M.J. Stillman, T. Nyokong, in: C.C. Leznoff (Ed.), *Lever ABP Phthalocyanines: Properties and Applications*, VCH Publishers, New York 1989, p. 133, (v. 1, Ch 3).
- [56] L. Li, J.F. Zhao, N. Won, H. Jin, S. Kim, J.Y. Chen, Quantum dot - aluminum phthalocyanine conjugates perform photodynamic reactions to kill cancer cells via fluorescence resonance energy transfer (FRET), *Nanoscale Res. Lett.* 7 (2012) 386–393.
- [57] M.H. Majles Ara, Z. Dehghani, R. Sahraei, A. Daneshfar, Z. Javadi, F. Divsar, Diffraction patterns and nonlinear optical properties of gold nanoparticles, *J. Quant. Spectrosc. Radiat. Transf.* 113 (2012) 366–372.
- [58] A.W. Snow, J.R. Griffith, N.P. Marullo, Syntheses and characterization of heteroatom-bridged metal-free phthalocyanine network polymers and model compounds, *Macromolecules* 17 (1984) 1614–1624.
- [59] R. Prabakaran, R. Kesavamoorthy, G.L.N. Reddy, F.P. Xavier, Structural investigation of copper phthalocyanine thin films using X-Ray diffraction, Raman scattering and optical absorption measurements, *Phys. Status Solidi* 229 (2002) 1175–1186.
- [60] R. Jenkins, R.L. Snyder, *Introduction to X-Ray Diffractometry*, Wiley and Sons, New York, 1996.
- [61] Y. Shimzu, T. Azumi, Mechanism of external heavy atom effect on intersystem crossing in fluid solutions. Analysis based on fluorescence decay data, *J. Phys. Chem.* 86 (1982) 22–26.
- [62] J. Li, A.V. Krasavin, L. Webster, P. Segovia, A.V. Zayats, D. Richards, Spectral variation of fluorescence lifetime near single metal nanoparticles, *Sci. Report.* 6 (2016) 21349–21358.
- [63] T.L. Jennings, M.P. Singh, G.F. Strouse, Fluorescent lifetime quenching near $d = 1.5$ nm gold nanoparticles: probing NSET validity, *J. Am. Chem. Soc.* 128 (2006) 5462–5467.
- [64] E. Dulkeith, A.C. Morteaux, T. Niedereichholz, T.A. Klar, J. Feldmann, S.A. Levi, F.C.J.M. van Veggel, D.N. Reinhoudt, M. Moller, D.I. Gittins, Fluorescence quenching of dye molecules near gold nanoparticles: radiative and nonradiative effects, *Phys. Rev. Lett.* 89 (2002) 203002–203006.
- [65] M.G. Debacker, O. Deleplanque, B. Van Vlierberge, F.X. Sauvage, A laser photolysis study of triplet lifetimes and of triplet–triplet annihilation reactions of phthalocyanines in DMSO solutions, *Laser Chem.* 8 (1988) 1–11.
- [66] Z. Watkins, J. Taylor, S. D'Souza, J. Britton, T. Nyokong, Fluorescence behaviour and singlet oxygen production of aluminium phthalocyanine in the presence of upconversion nanoparticles, *J. Fluoresc.* 25 (2015) 1417–1429.
- [67] D.O. Oluwole, E. Prinsloo, T. Nyokong, Photophysicochemical properties of nanoconjugates of zinc(II) (2(3)-mono-2-(4-oxy)phenoxy)acetic acid phthalocyanine with cysteamine capped silver and silver–gold nanoparticles, *Polyhedron* 119 (2016) 434–444.
- [68] A.M. Alkilany, P.K. Nagaria, C.R. Hexel, T.J. Shaw, C.J. Murphy, M.D. Wyatt, Cellular uptake and cytotoxicity of gold nanorods: molecular origin of cytotoxicity and surface effects, *Small* 5 (2009) 701–708.
- [69] A.M. Alkilany, L.B. Thompson, S.P. Boulos, P.N. Sisco, C.J. Murphy, Gold nanorods: their potential for photothermal therapeutics and drug delivery, tempered by the complexity of their biological interactions, *Adv. Drug Deliv. Rev.* 64 (2012) 190–199.
- [70] Y. Zhang, D. Xu, W. Li, J. Yu, Y. Chen, Effect of size, shape, and surface modification on cytotoxicity of gold nanoparticles to Human HEP-2 and Canine MDCK cells, *J. Nanomater.* 2012 (2012) 1–7.
- [71] H.J. Parab, H.M. Chen, T.C. Lai, J.H. Huang, P.H. Chen, R.S. Liu, M. Hsiao, C.H. Chen, D.P. Tsai, Y.K. Hwu, Biosensing, cytotoxicity, and cellular uptake studies of surface-modified gold nanorods, *J. Phys. Chem. C* 113 (2009) 7574–7578.
- [72] S. Manohar, R. Rayavarapu, W. Petersen, T.G. van Leeuwen, Cell viability studies of PEG-thiol treated gold nanorods as optoacoustic contrast agents, *SPIE Proc.* 7177 (2009), 71772D.
- [73] A.P. Leonov, J. Zheng, J.D. Clogston, S.T. Stern, A.K. Patri, A. Wei, Detoxification of gold nanorods by treatment with polystyrene sulfonate, *ACS Nano* 2 (2008) 2481–2488.
- [74] M.F. Tsai, S.H. Chang, F.Y. Cheng, V. Shanmugam, Y.S. Cheng, C.H. Su, C.S. Yeh, Au nanorod design as light-absorber in the first and second biological near-infrared windows for in vivo photothermal therapy, *ACS Nano* 7 (2013) 5330–5342.
- [75] L. Xing, B. Chen, D. Li, W. Wu, Z. Ying, Gold nanospheres enhanced photothermal therapy in a rat model, *Lasers Surg. Med.* (2018) <https://doi.org/10.1002/lsm.22793>.